marine drugs

MDPI

Article

Concise Synthesis and Biological Evaluation of a Phorbazole Analogue-B1 Identifies a Multi-Kinase Inhibitor with Anti-AML Activity

Xiang Chen [1,2], Liting Zhang [2], Jinqi Huang [2,3], Mingzhi Su [2,*], Yuewei Guo [2,4,*] and Xin Jin [2,*]

1 School of Pharmacy, Shandong Second Medical University, Weifang 261053, China; 19561429683@163.com
2 Shandong Laboratory of Yantai Drug Discovery, Bohai Rim Advanced Research Institute for Drug Discovery, Yantai 264117, China; zlt142301@163.com (L.Z.); 19863831618@163.com (J.H.)
3 School of Pharmacy, Shandong First Medical University & Shandong Academy of Medical Sciences, Jinan 250117, China
4 School of Medicine, Shanghai University, Shanghai 200444, China
* Correspondence: mzsu@baridd.ac.cn (M.S.); ywguo@simm.ac.cn (Y.G.); xjin@baridd.ac.cn (X.J.)

Abstract

Phorbazoles are bioactive marine alkaloids whose development is hampered by limited supply. We report a concise synthesis of the deschloro-phorbazole core via an optimized iodine-catalyzed oxazole annulation (56% yield). This route enabled efficient access to the scaffold and the preparation of analog **B1**. **B1** showed nanomolar cytotoxicity (IC_{50} = 0.04 μM) against MV4-11 leukemia cells by inducing G0/G1 arrest (via cyclin D1/CDK6 downregulation) and apoptosis. As a multi-kinase inhibitor, **B1** also potently inhibited endothelial network formation and migration, demonstrating anti-angiogenic activity. This work provides an efficient synthetic strategy and identifies **B1** as a promising dual-function anticancer lead compound.

Keywords: phorbazole analogs; concise synthesis; anti-angiogenic activity; multi-kinase inhibitor

1. Introduction

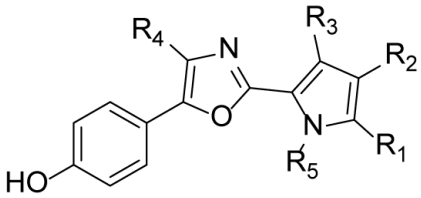
Marine alkaloids derived from oxazole-heterocycles constitute a significant class of natural products, often associated with potent biological activities [1,2]. Among these, the phorbazoles (A–D) (Figure 1) represent a distinctive family of polychlorinated pyrrole-oxazole metabolites first isolated from the marine sponge *Phorbas aff. clathrata* in 1994 [3]. They are historically notable as the first natural products identified to contain a 2-(2′-pyrrolyl)oxazole moiety and the first examples of naturally occurring chlorinated pyrroles. Although initial claims suggested immuno-modulatory activity for certain phorbazoles, this potential has not yet been substantiated by published studies [3]. Subsequent investigations led to the isolation of further analogs, such as phorbazoles E (9-chloro-phorbazole D) and F (N-methyl-phorbazole A) (Figure 1), from the nudibranch *Aldisa andersoni* [4]. Both compounds demonstrated significant feeding-deterrent activity against generalist predators and exhibited promising in vitro growth inhibitory (cytostatic) activity against a panel of human cancer cell lines (A549, MCF-7, SKMEL-28, Hs683 and U373), with IC_{50} values in the low micromolar range (18–34 μM) [4]. More recent studies have extended their pharmacological profile, with several derivatives based on the phorbazole scaffold being reported as inhibitors of HDACs (histone deacetylases) and MNKs (MAP kinase-interacting kinases), highlighting their potential as multitarget anticancer agents [5,6].

Check for updates

Academic Editor: Marialuisa Menna

Received: 8 January 2026
Revised: 25 January 2026
Accepted: 29 January 2026
Published: 2 February 2026

Copyright: © 2026 by the authors. Licensee MDPI, Basel, Switzerland. This article is an open access article distributed under the terms and conditions of the Creative Commons Attribution (CC BY) license.



Phorbazole A: R_1=H, R_2=R_3=R_4=Cl, R_5=H
Phorbazole B: R_1=R_2=R_3=Cl, R_4=R_5=H
Phorbazole C: R_1=R_4=H, R_2=R_3=Cl, R_5=H
Phorbazole D: R_1=R_2=R_4=H, R_3=Cl, R_5=H
Phorbazole E: R_1=R_2=H, R_3=R_4=Cl, R_5=H
Phorbazole F: R_1=H, R_2=R_3=R_4=Cl, R_5=CH_3

Figure 1. The structures of phorbazoles A–F.

Despite this therapeutic promise, the detailed biological evaluation and structure-activity relationship (SAR) studies of phorbazoles are severely constrained by their scarce natural abundance. Total synthesis thus emerges as an indispensable tool to address this supply bottleneck and enable systematic structural diversification. Early synthetic endeavors, such as the Robinson–Gabriel cyclodehydration route to phorbazole C, established foundational access but were often characterized by extended sequences (e.g., nine steps) and moderate overall yields (e.g., 17%) [7,8]. Subsequent strategies, including the use of pre-halogenated oxazole precursors, have achieved improvements but may lack convergence or flexibility for broad analog preparation.

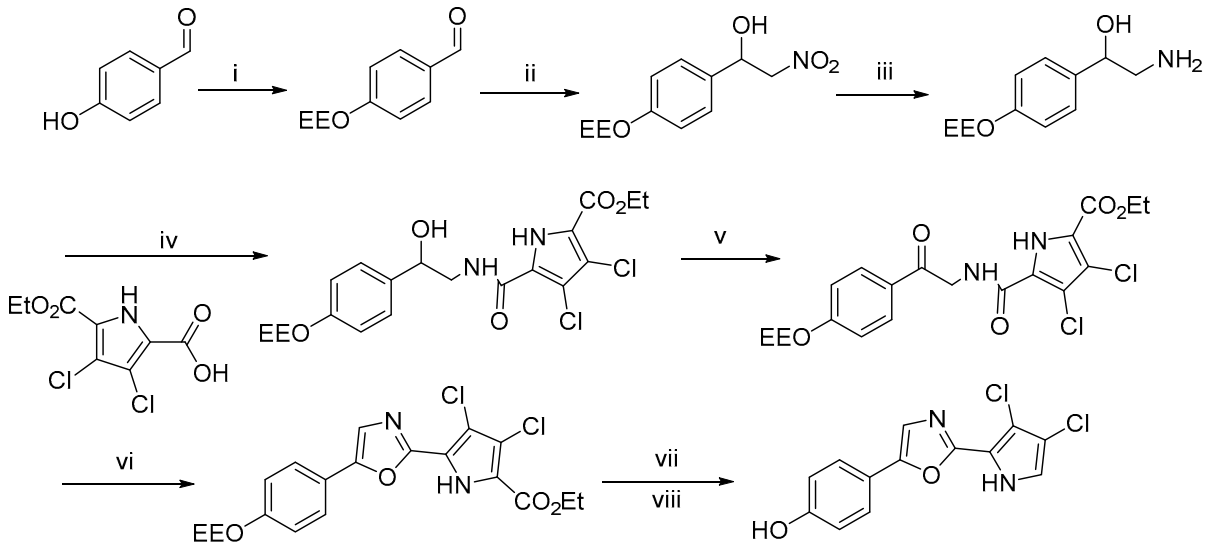
In our own research efforts, we have previously disclosed the total synthesis of a series of deschloro derivatives of phorbazole C and evaluated their inhibitory activity against MNKs [6]. While this work provided initial insights into the pharmacological potential of the phorbazole scaffold, the synthetic route employed was notably lengthy and proceeded in suboptimal yield. These limitations rendered the approach impractical for generating the diverse and complex compound libraries required for deeper mechanistic studies and comprehensive SAR exploration.

Therefore, the development of a concise, convergent, and efficient synthetic strategy remains a critical objective. Such a strategy, minimizing synthetic steps while maximizing overall yield and operational simplicity, is paramount. It would not only provide practical access to phorbazole C itself but, more importantly, serve as a robust and adaptable platform for the rapid assembly of diverse analog libraries. This would accelerate the exploration of the phorbazole pharmacophore, facilitating the optimization of cytotoxic potency and selectivity. This work details our efforts toward achieving such a concise total synthesis of phorbazole C and the application of this methodology to prepare novel derivatives for biological investigation.

2. Results

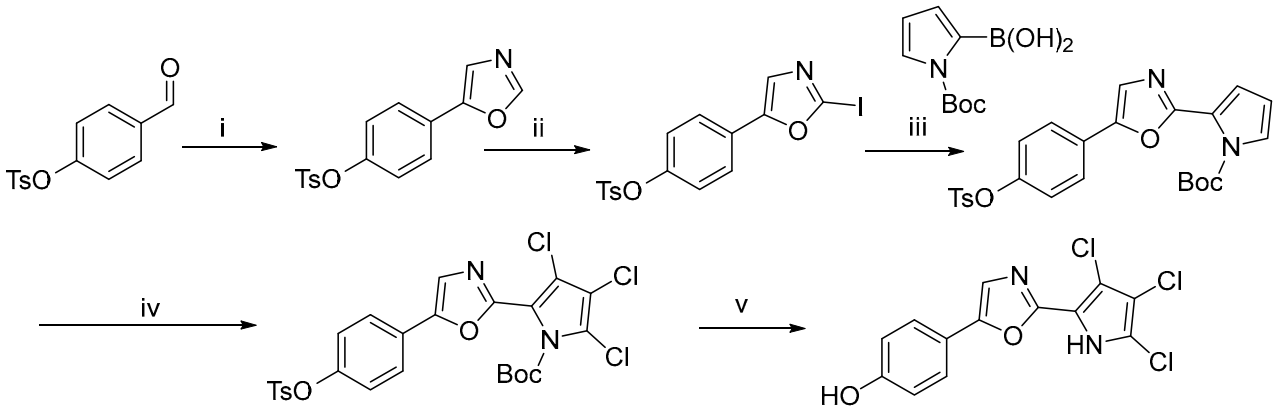
2.1. Previous Total Synthetic Route

In 2001, Alexander Radspieler and Jürgen Liebscher reported a synthetic route to Phorbazole C starting from 4-hydroxybenzaldehyde [7] (Scheme 1). The target compound was obtained in nine steps with an overall yield of 18%. 4-hydroxybenzaldehyde was protected with ethoxyethene, followed by Henry reaction, nitro reduction, amide condensation, Dess–Martin oxidation, a modified Wipf reaction, and protecting group removal to afford the target compound, Phorbazole C.



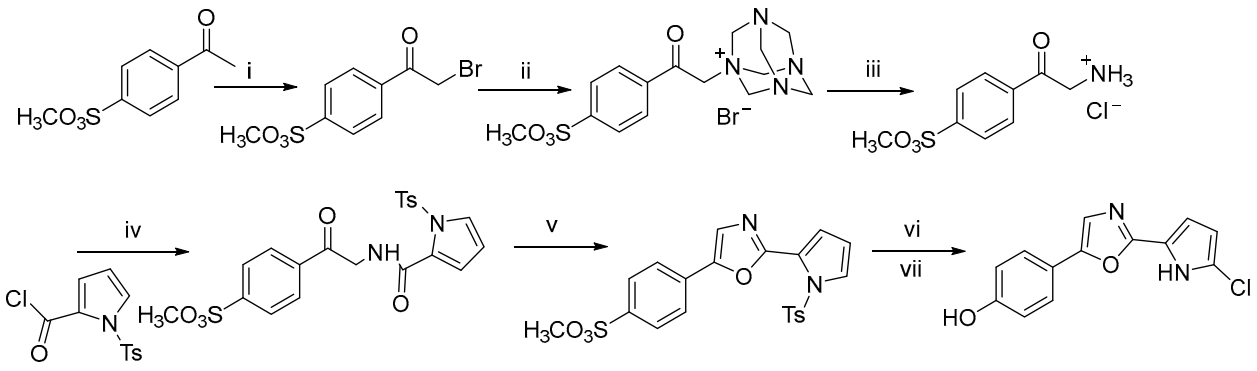
Scheme 1. Total synthesis of Phorbazole C [a]. [a] Reagents and conditions: (i) EtO-$CHCH_2$, MOM-Cl[cat], Et_2O, 78%; (ii) $MeNO_2$, Et_3N, DMSO, rt, 84%; (iii) H_2, Pd/C, rt, 88%; (iv) DCC, HOBt, DIPEA, DCM, rt, 65%; (v) DMP, DCM, rt, 98%; (vi) PPh_3, C_2Cl_6, NEt_3, DCM, rt, 87%; (vii) HCl, rt, 77%; (viii) NaOH, EtOH, rf, 84%; $NH_2C_2H_4OH$, 170 °C, 85%.

Subsequently, in 2020, Annette Bayer et al. reported a novel synthetic route to phorbazole compounds [9] (Scheme 2). Starting from 4-hydroxybenzaldehyde, phorbazole B was obtained in seven steps with an overall yield of 19%. This route involved initial protection of the hydroxyl group with a tosyl (Ts) group, followed by construction of the oxazole ring via a Van Leusen reaction. Subsequent steps included iodination, a Suzuki coupling reaction, chlorination, and final deprotection to afford the target compound, phorbazole B (Scheme 2).



Scheme 2. Total synthesis of phorbazole B [a]. [a] Reagents and conditions: (i) TosMIC, DBU, DME, 70%; (ii) LiHMDS, THF, −78 °C; I_2, −78 °C-rt, 12%; (iii) $PdCl_2$ (dppf), Cs_2CO_3, dioxane/H_2O, 75%; (iv) NCS, Ph_3PS, DMC, −20 °C-rt, 73%; (v) NaOH, EtOH, 87%.

In 2022, David J. Young et al. reported a novel synthetic method that afforded a new compound, phorbazole G, and its derivatives in seven steps with overall yields ranging from 26% to 52% [10]. This route is similar to the one previously reported by Alexander Radspieler and Jürgen Liebscher, utilizing a Delepine amine reaction to construct the key amine intermediate. Subsequently, the target compounds were obtained through a sequence of amide condensation, cyclization, chlorination, and final deprotection (Scheme 3).



Scheme 3. Total synthesis of a new phorbazole (phorbazole G) [a]. [a] Reagents and conditions: (i) Br, Et_2O/dioxane, rt, 96%; (ii) hexamethylenetetramine, CH_3Cl_3, rt, 94%; (iii) HCl, MeOH, rt, 24 h, 94%; (iv) Pyridine, rt, 2 d, 72%; (v) $POCl_3$, 2 h, 69%; (vi) NaOH, MeOH, reflux, 68%; (vii) SO_2Cl_2, Et_2O.

2.2. Our Total Synthetic Route

Previous synthetic routes can be summarized as first obtaining deschloro-phorbazole, followed by chlorination reactions using different reagents to control the number and position of chlorine atoms, thereby yielding Phorbazoles A–G (Figure 2A). Therefore, the key to reducing reaction steps and improving yields lies in how to efficiently and rapidly access the deschloro-phorbazole compound. In 2013, Chi Zhang reported a method for synthesizing oxazole rings using α-bromoketones and benzylamine derivatives in DMF under the catalysis of iodine and potassium carbonate (Figure 2B) [11]. This method enables the one-step preparation of 2,5-diaryl-substituted oxazoles. Consequently, we introduced this approach for synthesizing deschloro-phorbazole. The results show that we successfully obtained the target compounds, but the yield was low, at only 20% (Figure 2C).

We hypothesized that the unprotected NH group on the pyrrole ring might lead to additional side reactions. Therefore, we modified the starting material, (1H-pyrrol-2-yl)methanamine. Using pyrrole-2-carbonitrile as the starting material, we first protected the NH group with a benzyl group, followed by reduction of the cyano group to a primary amine using lithium aluminum hydride. Subsequently, this intermediate was reacted with 2-bromo-1-(4-hydroxyphenyl)ethanone in the presence of iodine and potassium carbonate to afford compound **3** in a one-step synthesis with a good yield of 56%. Finally, removal of the benzyl group yielded the target compound, deschloro-phorbazole (Scheme 4). Starting from compound **3**, chlorination was carried out on the pyrrole ring using N-chlorosuccinimide (NCS) under controlled conditions to introduce chlorine atoms at specific positions. However, we did not obtain any desired products. The reaction failure may stem from the fact that under Ph_3PS catalysis, NCS can chlorinate multiple positions on both the pyrrole and benzene rings [12]. This process occurs rapidly, making it difficult to achieve site-selective control. Therefore, within our reaction system, further optimization of conditions is required to selectively obtain the target compound.

Subsequently, starting from compound **1** and using an excess of NCS (N-chlorosuccinimide), only compound **4** was obtained, with no mono- or trichlorinated products detected when controlling the equivalents of NCS. The cyano group in compound **4** was then reduced with lithium aluminum hydride (LAH), and the resulting intermediate was cyclized with 2-bromo-1-(4-hydroxyphenyl)ethanone to afford the disubstituted oxazole compound **6**. Finally, removal of the benzyl protecting group yielded the target compound, phorbazole C (Scheme 5).

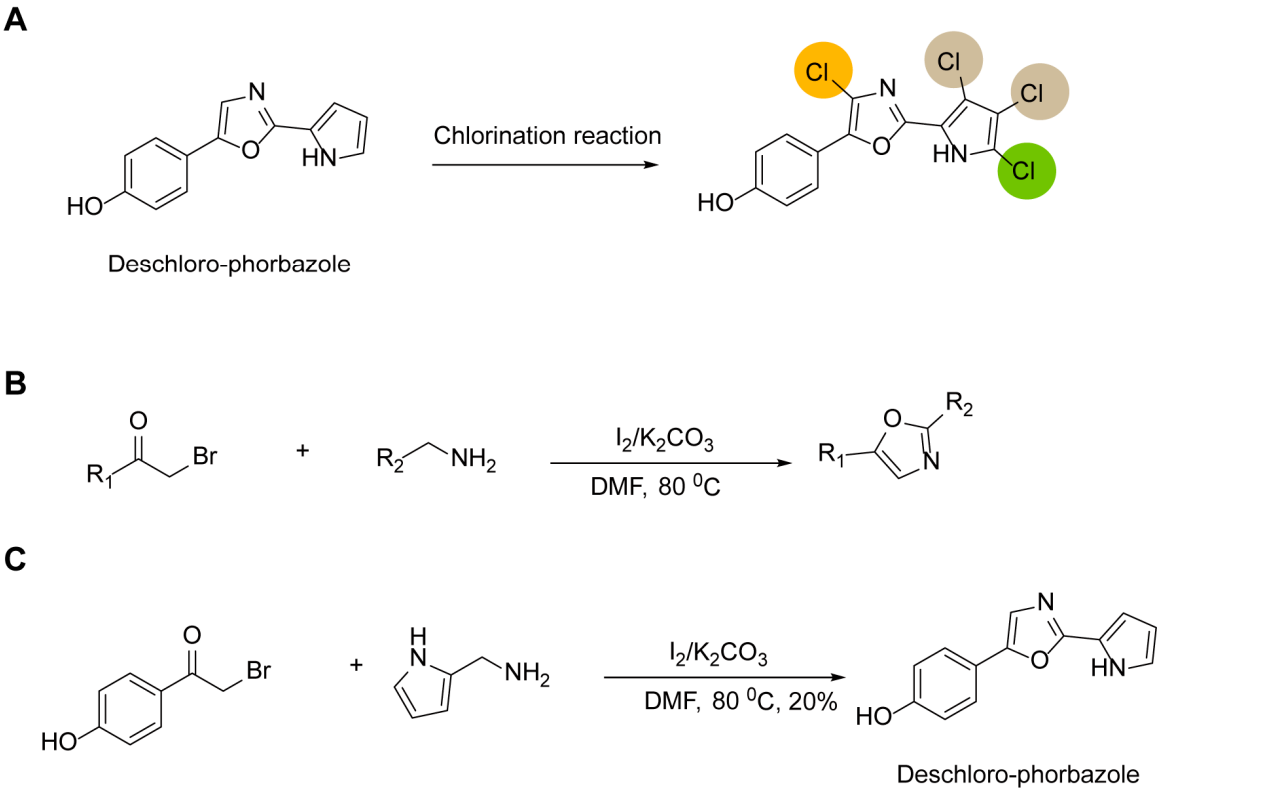
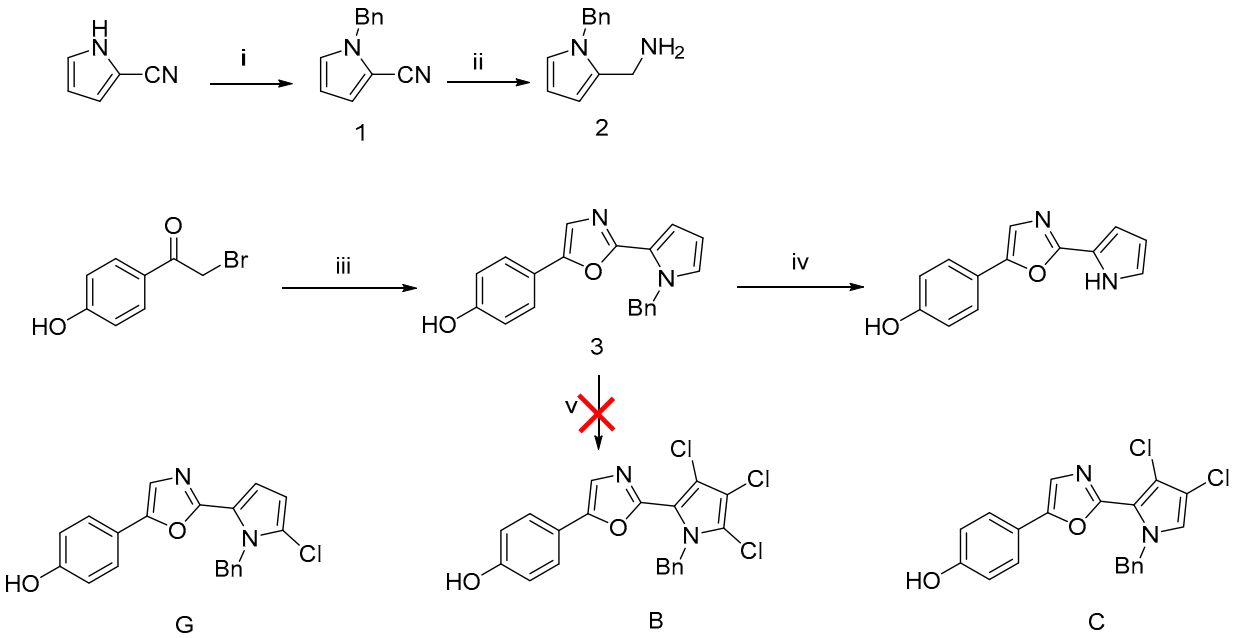
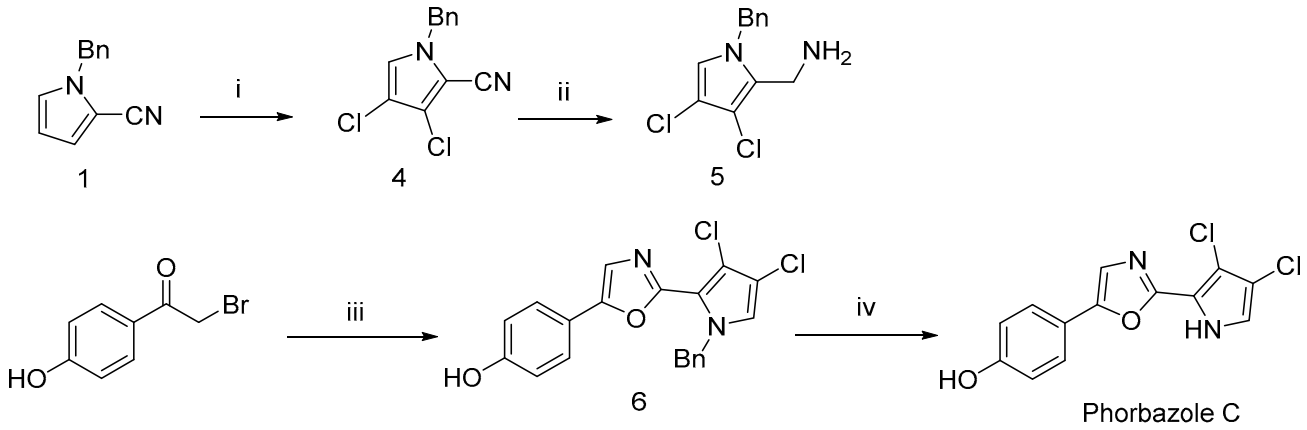


Figure 2. Simplified synthesis steps of the phorbazole series of compounds: (**A**) a general strategy for the synthesis of phorbazole series compounds; the chlorine atoms are color-coded to represent different compounds. (**B**) a novel synthetic route for 2,5-diaryl-substituted oxazoles; (**C**) a concise synthetic route for deschloro-phorbazole.

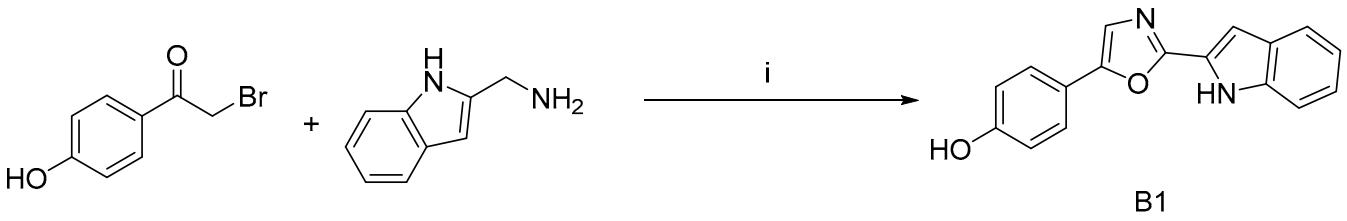


Scheme 4. Modified concise synthetic route to deschloro-phorbazole [a]. [a] Reagents and conditions: (i) NaH, BnBr, THF, 96%; (ii) $LiAlH_4$, THF, rt, 84%; (iii) **2**, I_2/K_2CO_3, DMF, 56%; (iv) H_2, Pd/C, 92%; (v) NCS, Ph_3PS, DCM, rt. Note: The red cross indicates that this route cannot be taken under the current conditions.

To expand the diversity of phorbazole compounds and demonstrate the utility of this one-step reaction in synthesis, we designed and synthesized a derivative of deschloro-phorbazole, compound **B1**, which can be obtained with a 30% yield (Scheme 6).



Scheme 5. Concise synthetic route to Phorbazole C [a]. [a] Reagents and conditions: (i) NCS, Ph_3PS, DCM, 90%; (ii) $LiAlH_4$, THF, rt, 84%; (iii) **5**, I_2/K_2CO_3, DMF, 56%; (iv) H_2, Pd/C, 92%.



Scheme 6. Synthetic route to compound **B1** [a]. [a] Reagents and conditions: (i) I_2/K_2CO_3, DMF, 80 °C, 30%.

2.3. Cytotoxic Activity and Kinase Inhibition Profile of **B1**

Consequently, we evaluated the cytotoxic activity of compounds (deschloro-phorbazole, compound **6**, phorbazole C, and **B1**) in AML MV4–11 cells (Table 1). The results indicated that **B1** exhibited significant inhibitory activity, with IC_{50} values of 0.04 μM. The compounds phorbazole C and deschloro-phorbazole exhibit similar cytotoxic activity with IC_{50} values of 0.65 μM and 0.52 μM, respectively, indicating that the chlorine atom does not significantly contribute to this activity. However, when the N-H group on the pyrrole ring is substituted, the cytotoxic activity decreases markedly. We further evaluated the selectivity profiles of compound **B1** against a panel of 82 kinases in vitro (Figure 3, Table S1). The results revealed that **B1** is a multi-kinase inhibitor, exhibiting potent inhibitory effects on PDGFRα, TRKB, GAK, MLK1, QIK, HGK, and MNK1/2 at a concentration of 1 μM.

Table 1. The IC_{50} values of selected compounds against MV4–11.

Compound	IC_{50} (μM)
deschloro-phorbazole	0.52
6	12.3
Phorbazole C	0.65
B1	0.04
Ara-C	1.9
Cyclophosphamide	>100

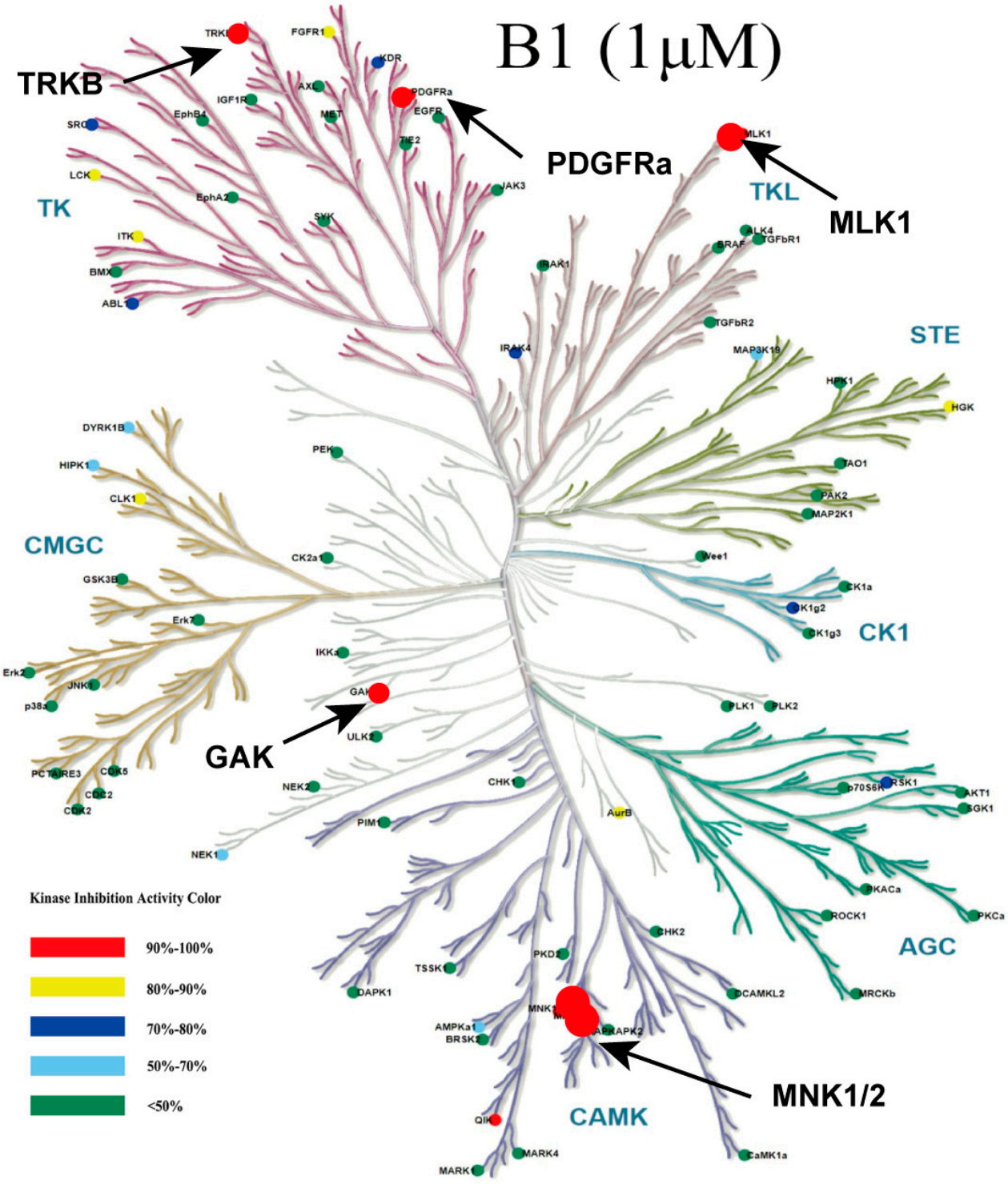


Figure 3. Kinome tree plot depicting the selectivity of **B1** across 82 kinases at 1 μM.

2.4. **B1** *Induces Cell Cycle Arrest and Promotes Apoptosis in AML Cells*

To investigate the effect of **B1** on the proliferative capacity of MV4–11 cells, we synchronized cultures and exposed them to 0.5 μM **B1** for 12, 24, 36, and 48 h. Flow-cytometric quantification of DNA content revealed a progressive, time-dependent accumulation of cells in the G0/G1 phase (from 60 ± 3% in the vehicle-treated group to 82 ± 2% after 36 h **B1** treatment), accompanied by a reciprocal decline in both S- and G2/M-phase populations (Figure 4A,B).

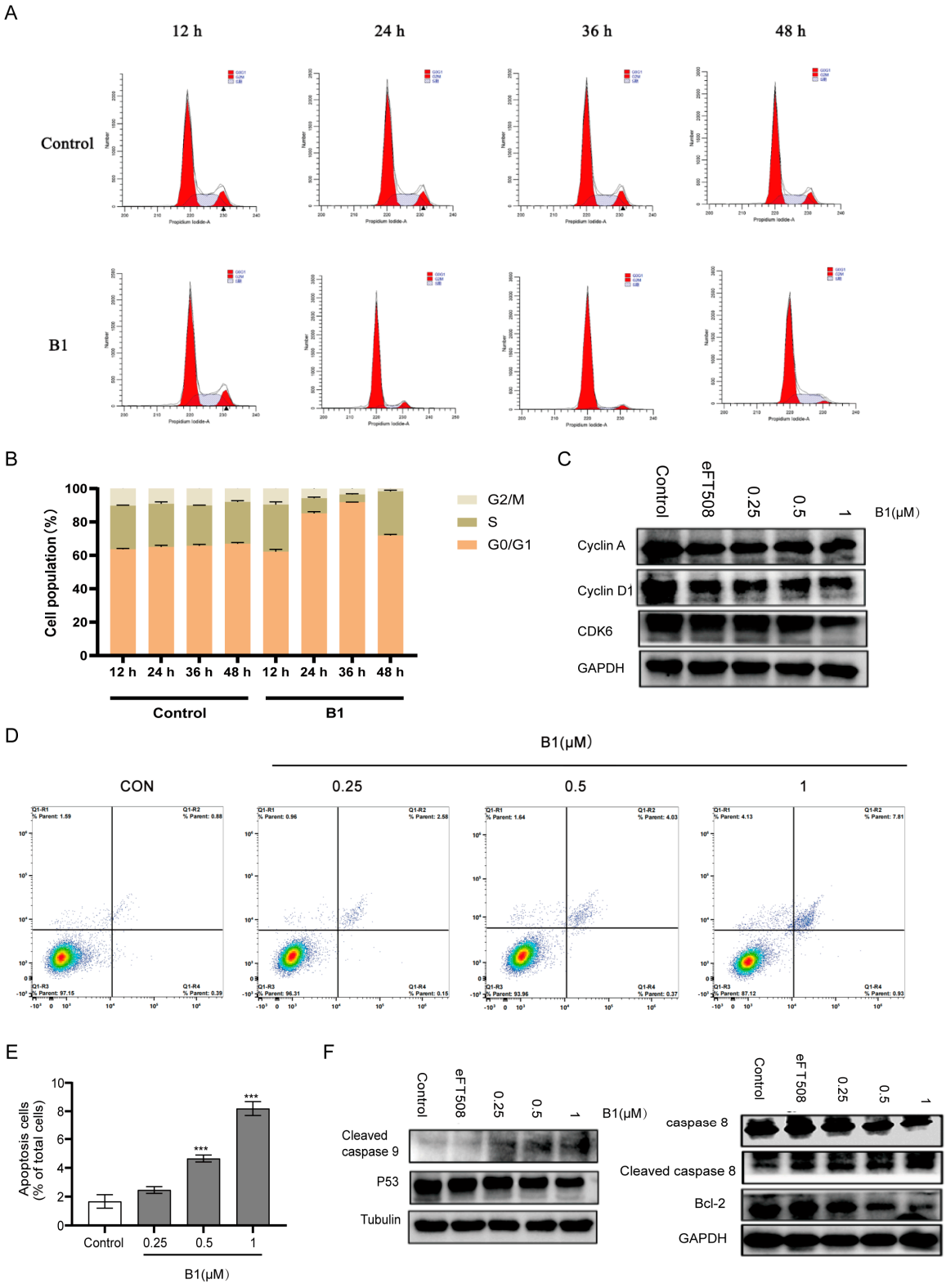


Figure 4. The effects of **B1** on cell cycle and apoptosis in MV4−11 cells. (**A**) Representative images of flow cytometry analysis in MV4−11 cells after the incubation of **B1** at the indicated concentrations for different times. (**B**) Quantification for (**A**). (**C**) Western blot analysis of MV4−11 cells treated with the indicated concentrations of **B1** for 24 h. DMSO and eFT508 (0.1 μM) are used as negative and positive controls, respectively. (**D**) Representative images of flow cytometry analysis in MV4−11 cells after the incubation of **B1** at the indicated concentrations for different times. (**E**) Quantification for (**D**). (**F**) Western blot analysis of MV4−11 cells treated with the indicated concentrations of **B1** for

24 h. DMSO and eFT508 (0.1 μM) are used as negative and positive controls, respectively. *p*-value is indicated by *** $p < 0.001$.

Consistent with a canonical G1 blockade, immunoblotting demonstrated a marked reduction in cyclin D1 and its catalytic partner CDK6 beginning as early as 12 h post-treatment (Figure 4C). Cyclin A, which accumulates during late G1 and S phases, was only modestly decreased, underscoring the specificity of the G1 arrest. Dose-escalation studies further revealed that cyclin D1 down-regulation occurred in a concentration-dependent manner (Figure 4D).

To determine whether **B1** also triggers programmed cell death, Annexin V/PI co-staining was performed. The proportion of late apoptotic/necrotic cells increased from 2 ± 1% under basal conditions to 8 ± 3% after treatment with 1 μM **B1** (Figure 4E). Western blot analysis of key apoptosis regulators showed a concentration-dependent activation of cleaved caspase-9, along with a reduction in total p53 protein levels and a pronounced decrease in the anti-apoptotic protein Bcl-2 (Figure 4F). The observed decrease in p53 is consistent with its role in the DNA damage response; upon activation, p53 can undergo post-translational modifications (e.g., phosphorylation) that may alter its electrophoretic mobility or antibody recognition, or it may be targeted for degradation in a feedback loop after initiating pro-apoptotic signaling [13]. This, together with caspase-9 cleavage and Bcl-2 downregulation, supports the induction of the intrinsic apoptotic pathway.

Collectively, these data indicate that **B1** exerts a dual anti-leukemic effect: (i) it enforces a stringent G0/G1 arrest by suppressing cyclin D1/CDK6 expression, and (ii) it activates the intrinsic apoptotic pathway through down-regulation of Bcl-2 and activation of caspase-9. Both phenotypes are consistent with inhibition of the MNK/eIF4E signaling axis, which governs cap-dependent translation of short-lived proteins such as cyclin D1 and Bcl-2 [14,15].

2.5. **B1** *Disrupts Endothelial Network Formation*

We noted that compound **B1** exhibits potent inhibitory activity on PDGFRα, KDR, and FGFR, which are known to promote angiogenesis by providing oxygen and nutrient supply in cancers [16,17]. Given its anti-proliferative and pro-apoptotic effects on tumor cells, we hypothesized that **B1** might also interfere with tumor-associated neovascularization. To evaluate this possibility, we exploited a well-established in vitro angiogenesis model in which human umbilical vein endothelial cells (HUVECs) form capillary-like networks on growth-factor-reduced Matrigel. HUVEC monolayers were pre-treated for 1 h with graded concentrations of **B1** (0.25, 1, and 4 μM) or vehicle, seeded onto Matrigel, and imaged at 3, 9, and 12 h under phase-contrast microscopy (Figure 5A).

Quantitative image analysis (number of meshes and master junction) revealed a time- and concentration-dependent disruption of tube formation (Figure 5B,C). While control cultures developed extensive interconnected networks by 12 h, **B1** caused a stepwise suppression of these parameters. At 4 μM, the number of meshes was reduced by 78 ± 5% ($p < 0.001$) and master junction by 75 ± 4% at 12 h, confirming potent anti-angiogenic activity (Figure 5B,C).

To determine whether the impaired network assembly resulted from an inhibition of endothelial motility, we performed a standardized wound-healing (scratch) assay. Confluent HUVEC monolayers were scratched and exposed to **B1** in complete medium. Wound closure was monitored for 24 h; 4 μM **B1** decreased migratory velocity by 62 ± 3% relative to vehicle ($p < 0.001$), whereas 0.25 and 1 μM also produced modest but significant reductions (Figure 5E). Notably, these concentrations did not affect cell viability within the assay window (Figure 5F), indicating that the anti-migratory effect was cytostatic rather than cytotoxic.

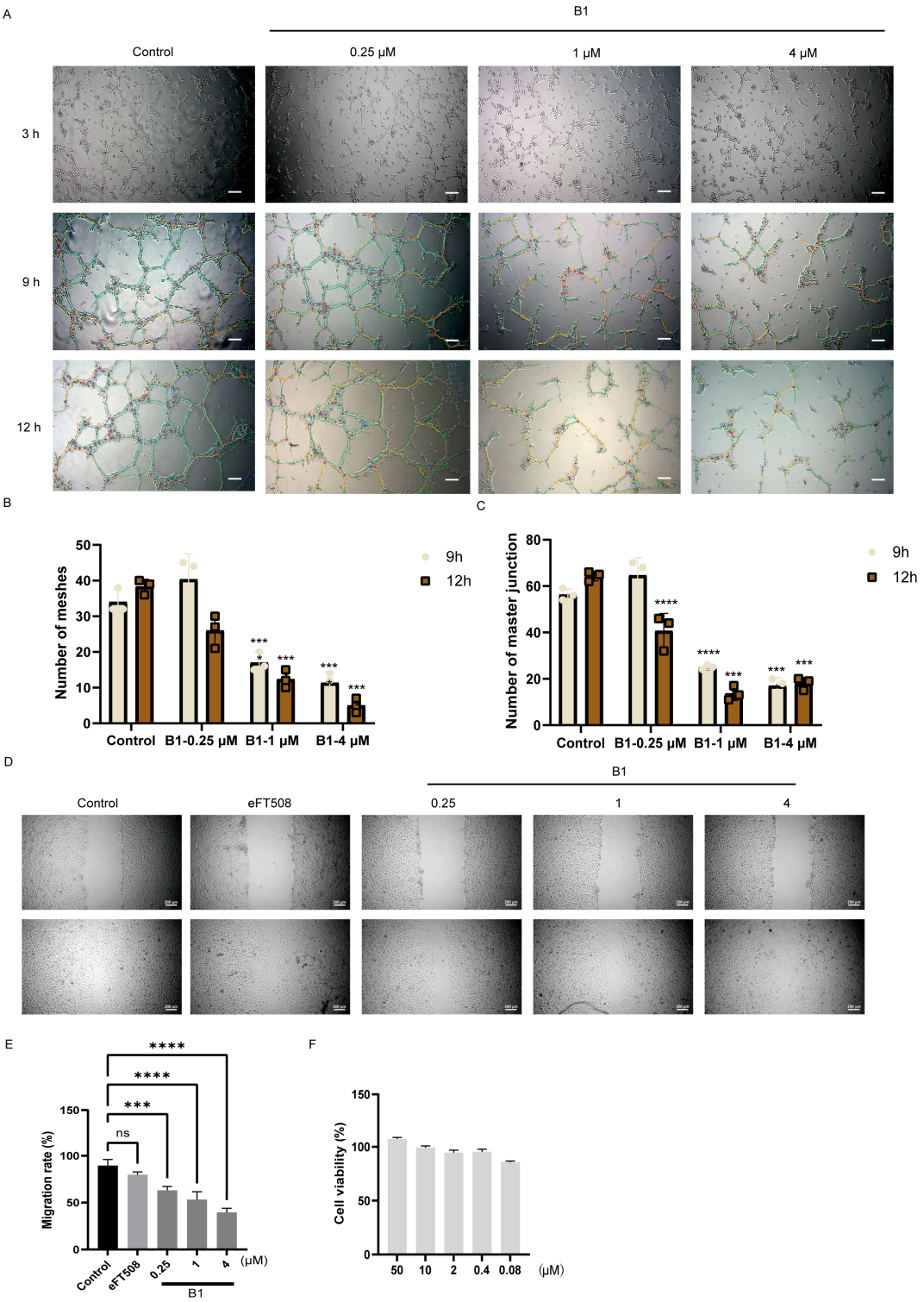


Figure 5. The effects of **B1** on angiogenesis of HUEVC cells. (**A**) The vascularization of HUEVC cells at different time points after treatment of **B1** at the indicated concentrations, scale bar, 200 μm. (**B**,**C**) Quantification of the number of meshes and master junctions for (**A**). (**D**) Migration of HUEVC cells treated with indicated compounds, scale bar, 200 μm. (**E**) Quantifying the migration rate for (**D**). (**F**) Cell viability of **B1** in HUEVC cells. *p*-values are indicated by * $p < 0.5$, *** $p < 0.001$, **** $p < 0.0001$; ns, not significance.

2.6. **B1** *Suppresses Tumor Growth in AML Xenograft Model*

Motivated by the potent anti-proliferative activity of **B1** against MV4−11 cells in vitro, we evaluated its therapeutic potential in an aggressive AML xenograft model. Cyclophos-

phamide (CTX, 40 mg/kg) was used as a positive control, which does not exhibit cytotoxic activity in vitro. Upon entering the human body, it is hydrolyzed by phosphamidase or phosphatase into the activated form, phosphoramide mustard, which is a nitrogen mustard derivative. It has a broad antitumor spectrum and is recognized as the first so-called "latentiated" broad-spectrum antitumor agent, effective against both leukemia and solid tumors. **B1** elicited a clear, dose-dependent suppression of tumor growth (Figure 6B,C). By day 14, the mean tumor weight in the vehicle group had reached 0.25 ± 0.13 g, whereas the 20 and 40 mg/kg **B1** groups exhibited weights of 0.14 ± 0.06 g and 0.11 ± 0.04 g, respectively, corresponding to tumor growth inhibition (TGI) rates of 44% ($p < 0.05$) and 55% ($p < 0.05$). Importantly, no significant body-weight loss (>5%) was observed throughout the treatment period, indicating that **B1** was well tolerated at both doses (Figure 6A).

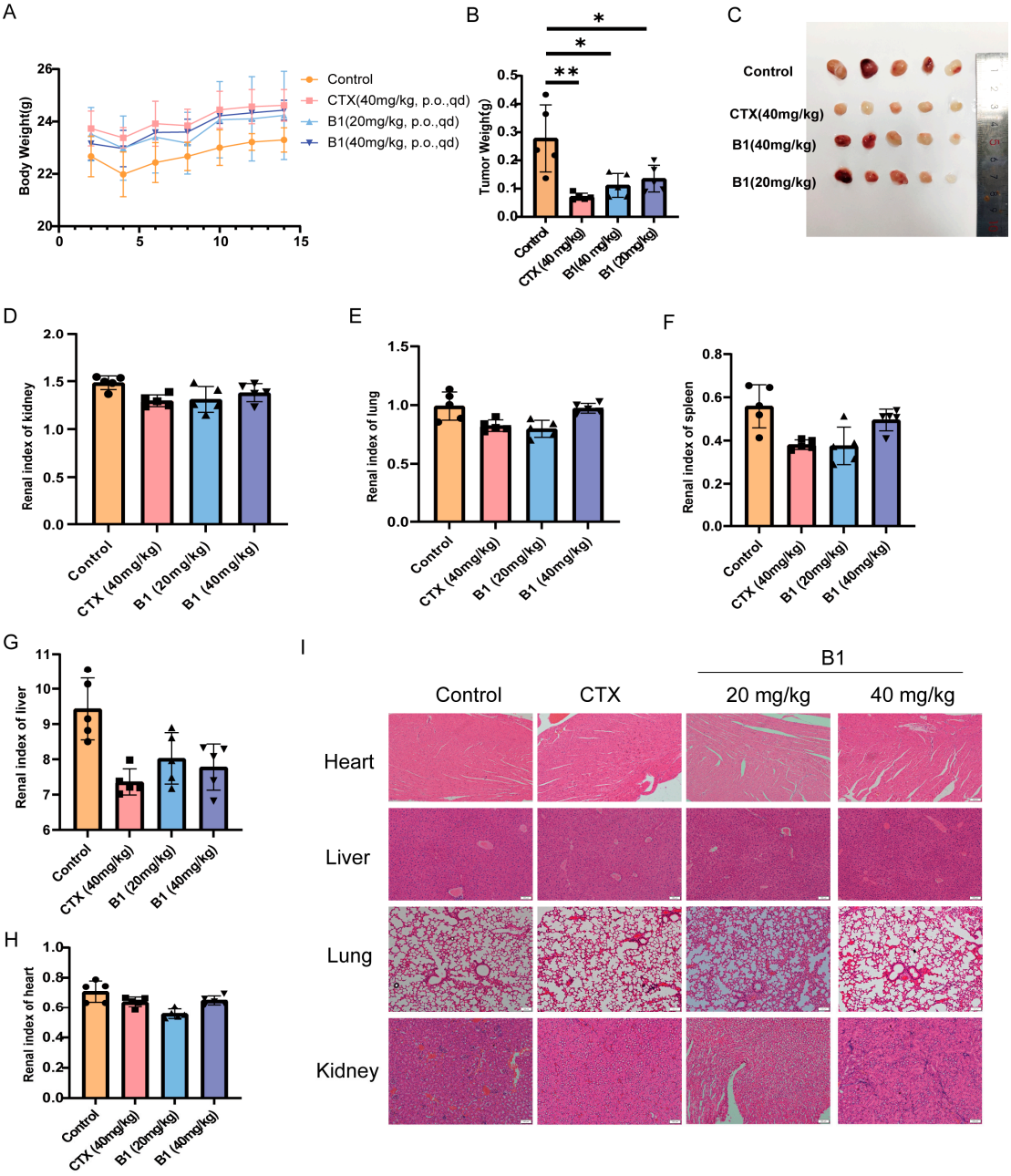


Figure 6. In vivo efficacy in the MV4−11 xenograft model following 14 days of oral gavage administration. (**A**) Mouse body weights. (**B**) Tumor weights. (**C**) Tumor diagrams from each group. (**D**–**H**) Indices

for the kidney, lung, spleen, liver, and heart. (**I**) Tissue samples from each group were stained for H&E, scale bar, 100 μm. *p*-values are indicated by * $p < 0.05$, ** $p < 0.01$. CTX (Cyclophosphamide) was used as a positive control.

Gross necropsy and histopathologic evaluation of major organs revealed no macroscopic abnormalities in the kidneys, lungs, and heart. H&E staining further confirmed the absence of inflammatory infiltrates, fibrosis, or tissue damage (Figure 6D–I). Interestingly, both **B1**-treated groups improve spleen and liver morphology compared to vehicle controls (Figure 6F,G), suggesting that **B1** may confer modest immunomodulatory or hepatoprotective effects under stress conditions.

Collectively, these data demonstrate that oral administration of **B1** achieves significant, dose-dependent antitumor efficacy against MV4-11 xenografts without eliciting overt systemic toxicity, thereby validating its potential for further pre-clinical development in AML therapy.

3. Discussion

This work successfully addresses a major bottleneck in phorbazole research—the lack of an efficient and adaptable synthetic route. By refining the one-step oxazole annulation reported by Chi Zhang et al., we developed a significantly improved synthesis of the deschloro-phorbazole core. The critical modification, involving N-benzyl protection of the pyrrole starting material, mitigated side reactions and increased the key cyclization yield to 56%, enabling practical access to this scaffold for the first time. Although our attempts at late-stage, regioselective chlorination of the pyrrole ring were unsuccessful, likely due to competing reactions at unprotected phenolic and pyrrolic sites, the developed route provides robust access to the deschloro framework, which serves as a versatile platform for diversification, as demonstrated by the synthesis of analog **B1.**

The biological characterization of **B1** reveals a compelling and multifaceted profile. Its potent anti-proliferative activity in MV4−11 cells is underpinned by a clear mechanistic duality: the induction of a stringent G0/G1 arrest and the activation of the intrinsic apoptotic pathway. The concomitant downregulation of cyclin D1 and Bcl-2, both proteins with short half-lives dependent on cap-dependent translation, strongly suggests that these effects are mediated through the inhibition of the MNK/eIF4E signaling axis, a hypothesis supported by the kinome scan identifying **B1** as a multi-kinase inhibitor with activity against MNK1/2. This aligns with the known role of MNK in regulating the translation of oncogenic mRNAs [18].

Perhaps more striking is the discovery of **B1**'s potent anti-angiogenic activity. Its ability to disrupt endothelial tube formation and migration at low micromolar concentrations, without inducing acute cytotoxicity, positions it as a direct inhibitor of pathological angiogenesis. This activity may be linked to its inhibition of receptor tyrosine kinases such as PDGFRα, KDR (VEGFR2), and FGFR, which are pivotal in angiogenic signaling. In solid tumors, anti-angiogenic therapy aims to starve the tumor by blocking the formation of new blood vessels that supply oxygen and nutrients [19,20]. However, in leukemia, the disease develops within the vascularized bone marrow niche rather than as an avascular solid mass [21,22]. Here, angiogenesis plays a distinct but critical role: leukemic cells alter the marrow microenvironment, promoting abnormal vessel growth that in turn supports leukemic stem cell survival, proliferation, and chemoresistance. Thus, while anti-angiogenic strategies in leukemia do not target a structural vascular network as in solid tumors, they disrupt a key component of the protective microenvironment that fosters disease progression and therapy resistance. The anti-angiogenic activity of **B1** may therefore provide a dual therapeutic advantage: direct cytotoxicity toward leukemic cells and suppression of the supportive vascular niche.

The dual capacity to simultaneously target leukemia cell proliferation/survival and the tumor vascular niche represents a significant advantage, potentially overcoming limitations of single-pathway inhibitors and suggesting utility in combating drug resistance.

4. Conclusions

In conclusion, this study established a concise and efficient synthetic foundation for the phorbazole class of natural products. This methodology facilitated the discovery of **B1**, a novel small molecule exhibiting a unique combination of potent multi-kinase inhibition, anti-leukemic efficacy, and anti-angiogenic activity. Our work validates the phorbazole scaffold as a promising source of pharmacologically active motifs and provides a new chemical entity for the development of multi-targeted anticancer therapies.

Future work will focus on further elucidating the mechanism of action and optimizing the activity profile of **B1**. This will involve structural refinement to deepen the understanding of its structure-activity relationships, evaluation of its in vivo efficacy across diverse AML models such as patient-derived xenografts, and systematic investigation into the specific contributions of its kinase targets to the observed anti-leukemic and anti-angiogenic phenotypes. Additionally, exploring the combination potential of **B1** with standard therapies will help clarify the cooperative mechanisms underlying its multi-target effects. These in-depth studies will strengthen the preclinical scientific foundation of **B1** and provide a rationale for developing novel multi-target strategies against AML and other angiogenesis-related disorders.

5. Materials and Methods

Compound synthesis. All reagents and solvents were purchased from Aladdin (Shanghai, China), Energy Chemical (Shanghai, China), Bide Chemical (Shanghai, China), or Tianjin Hengxing Chemical (Tianjin, China) and were of reagent-grade quality. All actions were carried out with continuous magnetic stirring in common glassware. Cooling of reactions was conducted with ice or an ice bath. ^{1}H and ^{13}C spectra were measured on a Bruker 600 spectrometer (^{1}H at 600 MHz and ^{13}C at 150 MHz) with tetramethylsilane (Me_4Si) as the internal standard, chemical shifts were reported as δ values (ppm) with $CDCl_3$ (^{1}H: δ = 7.26, ^{13}C: δ = 77.16) or DMSO-d_6 (^{1}H: δ = 2.50, ^{13}C: δ = 39.52) as the internal standard. Mass spectra were measured on a Q-Tof Global mass spectrometer. Column chromatography was performed on silica gel (200–300 mesh, Qingdao, China).

4-(2-(1H-pyrrol-2-yl)oxazol-5-yl)phenol (Deschloro-phorbazole). Iodine (710 mg, 2 equiv.) was added to the mixture of 2-Bromo-4′-hydroxyacetophenone (300 mg, 1 equiv.), (1H-pyrrol-2-yl)methanamine (204 mg, 1.2 equiv.) and K_2CO_3 (774 mg, 4 equiv.) in 2 mL of DMF, and then the mixture was stirred at 80 °C. After the reaction was complete by TLC analysis, EA was added to dilute the reaction mixture, followed by the treatment of sat. $Na_2S_2O_3$ solution to quench the reaction. The organic layer was separated, washed in water, and dried over anhydrous Na_2SO_4. After the removal of the solvent in vacuo, the residue was purified by flash column chromatography with PE/EA (2:1) to afford the compound in 20% yield. ^{1}H NMR (600 MHz, DMSO-d_6) δ 11.85 (s, 1H), 9.78 (s, 1H), 7.59 (d, J = 8.6 Hz, 2H), 7.45 (s, 1H), 6.97 (d, J = 2.1 Hz, 1H), 6.87 (d, J = 8.6 Hz, 2H), 6.73 (dt, J = 3.7, 1.8 Hz, 1H), 6.20 (q, J = 2.4 Hz, 1H); HRMS calcd for ($C_{13}H_{10}N_2O_2$ + H) + 227.0742, found 227.0740.

1-benzyl-1H-pyrrole-2-carbonitrile (1). To a solution of 1 g of 1H-pyrrole-2-carbonitrile in THF was added NaH (869 mg) under an ice bath. After stirring for 30 min, benzyl bromide (3.7 g) was added. The reaction mixture was then stirred at room temperature for 6 h, quenched with water, and extracted with ethyl acetate. The combined organic layers were concentrated, and the residue was purified by column chromatography to afford 1.8 g

of the product as an oily liquid in 91% yield. ^{1}H NMR (600 MHz, $CDCl_3$) δ 7.34–7.32 (m, 3H), 7.17 (d, *J* = 6.0 Hz, 2H), 6.83–6.80 (m, 2H), 6.19 (dd, *J* = 2.9, 2.7 Hz, 1H), 5.27 (s, 2H).

(1-benzyl-1H-pyrrol-2-yl)methanamine (2). Compound **1** was dissolved in tetrahydrofuran. Under a nitrogen atmosphere, lithium aluminum hydride (2.0 equiv.) was added at 0 °C. The reaction mixture was stirred at this temperature for 1 h, then allowed to warm to room temperature, and stirred for an additional 3 h. After the starting material was consumed (monitored by TLC), the reaction was carefully quenched with water. The resulting mixture was filtered to remove insoluble solids, and the filtrate was extracted with DCM. The combined organic extracts were concentrated under reduced pressure, and the crude product was used directly in the next step without further purification.

4-(2-(1-benzyl-1H-pyrrol-2-yl)oxazol-5-yl)phenol (3). Iodine (1.06 g, 2.0 equiv.) was added to the mixture of 2-Bromo-4′-hydroxyacetophenone (454 mg, 1.0 equiv.), compound **2** (433 mg, 1.2 equiv.), and K_2CO_3 (1.16 g, 4.0 equiv.) in 15 mL of DMF, and then the mixture was stirred at 80 °C. After the reaction was complete by TLC analysis, EA was added to dilute the reaction mixture, followed by the treatment of sat. $Na_2S_2O_3$ solution to quench the reaction. The organic layer was separated, washed in water, and dried over anhydrous Na_2SO_4. After the removal of the solvent in vacuo, the residue was purified by flash column chromatography with PE/EA (2:1) to afford the compound in 56% yield. ^{1}H NMR (600 MHz, DMSO-d_6) δ 9.77 (s, 1H), 7.54–7.52 (m, 2H), 7.45 (s, 1H), 7.29–7.27 (m, 3H), 7.22 (dd, *J* = 7.8, 1.7 Hz, 1H), 7.17 (t, *J* = 2.2 Hz, 1H), 7.12–7.09 (m, 2H), 6.89 (dd, *J* = 3.8, 1.8 Hz, 1H), 6.85–6.84 (m, 2H), 6.25 (dd, *J* = 3.8, 2.6 Hz, 1H), 5.73 (s, 2H). ^{13}C NMR (150 MHz, DMSO-d_6) δ 158.18, 154.93, 149.60, 139.48, 129.02, 128.91, 127.58, 127.01, 125.95, 121.35, 120.65, 119.04, 116.32, 112.86, 109.36, 51.25. HRMS calculated for (M + H) + 317.1213, found 317.1210.

1-benzyl-3,4-dichloro-1H-pyrrole-2-carbonitrile (4). Using compound **1** as the starting material, 3 equivalents of NCS were added and stirred in DCM at room temperature overnight. The next day, the mixture was washed with water, and the organic layer was separated. It was then washed with saturated brine, concentrated, and purified by column chromatography to give compound **4** as an oil in 80% yield. ^{1}H NMR (600 MHz, $CDCl_3$) δ 7.41–7.34 (m, 3H), 7.25–7.23 (m, 2H), 6.83 (s, 1H), 5.28 (s, 2H).

4-(2-(1-benzyl-3,4-dichloro-1H-pyrrol-2-yl)oxazol-5-yl)phenol (6). Iodine (2.0 equiv.) was added to the mixture of 2-Bromo-4′-hydroxyacetophenone (1.0 equiv.), (1H-Indol-2-yl)methanamine (1.2 equiv.) and K_2CO_3 (4.0 equiv.) in 2 mL of DMF, and then the mixture was stirred at 80 °C. After the reaction was complete by TLC analysis, EA was added to dilute the reaction mixture, followed by the treatment of sat. $Na_2S_2O_3$ solution to quench the reaction. The organic layer was separated, washed in water, and dried over anhydrous Na_2SO_4. After the removal of the solvent in vacuo, the residue was purified by flash column chromatography with PE/EA (2:1) to afford the compound in 56% yield. ^{1}H NMR (600 MHz, DMSO-d_6) δ 9.95 (s, 1H), 7.58–7.56 (m, 2H), 7.51 (s, 1H), 7.32 (dd, *J* = 8.3, 7.0 Hz, 2H), 7.27–7.23 (m, 1H), 7.18 (s, 1H), 7.07–7.05 (m, 2H), 6.88–6.85 (m, 2H), 5.85 (s, 2H). HRMS calculated for (M + H) + 385.0505, found 385.0500.

4-(2-(3,4-dichloro-1H-pyrrol-2-yl)oxazol-5-yl)phenol (Phorbazole C). The compound **6** was dissolved in methanol and reacted under a hydrogen atmosphere with palladium on carbon for 12 h. After filtration to remove the palladium on carbon, the solvent was evaporated, and purification by column chromatography afforded a pale-yellow solid in 92% yield. ^{1}H NMR (600 MHz, DMSO-d_6) δ 13.12 (s, 1H), 9.81 (s, 1H), 7.63–7.61 (m, 2H), 7.51 (s, 1H), 6.88–6.86 (m, 3H). ^{13}C NMR (150 MHz, DMSO-d_6) δ 157.87, 153.04, 150.10, 125.65, 121.08, 118.88, 118.48, 115.84, 114.74, 109.14. HRMS calculated for (M + H) + 295.0035, found 295.0032.

4-(2-(1H-indol-2-yl)oxazol-5-yl)phenol (B1). Iodine was added to the mixture of 2-Bromo-4′-hydroxyacetophenone, (1H-Indol-2-yl)methanamine, and K_2CO_3 in 2 mL of DMF, and then the mixture was stirred at 80 °C. After the reaction was complete by TLC analysis, EA was added to dilute the reaction mixture, followed by the treatment of sat. $Na_2S_2O_3$ solution to quench the reaction. The organic layer was separated, washed in water, and dried over anhydrous Na_2SO_4. After the removal of the solvent in vacuo, the residue was purified by flash column chromatography with PE/EA (2:1) to afford the compound in 30% yield. ^{1}H NMR (600 MHz, DMSO-d_6) δ 11.96 (s, 1H), 9.86 (s, 1H), 7.69–7.67 (m, 2H), 7.65–7.62 (m, 2H), 7.47 (dq, *J* = 8.1, 0.9 Hz, 1H), 7.21 (ddd, *J* = 8.2, 6.9, 1.2 Hz, 1H), 7.12 (dd, *J* = 2.1, 0.9 Hz, 1H), 7.07 (ddd, *J* = 8.0, 6.9, 1.0 Hz, 1H), 6.92–6.89 (m, 2H). ^{13}C NMR (150 MHz, DMSO-d_6) δ 158.46, 155.14, 151.25, 137.76, 128.14, 126.27, 125.84, 123.74, 122.07, 121.47, 120.47, 119.00, 116.39, 112.43, 102.79. HRMS calculated for (M + H) + 277.0972, found 277.0984.

Kinase Selectivity Assays: Compound **B1** was tested at 1 μM against a panel of 82 kinases through the commercial profiling service from ICE Bioscience (Beijing, China).

Cell Culture: HUEVC and MV4–11 cells were purchased from Procell Life Science & Technology Co., Ltd. (Wuhan, China). The HUEVC cells were cultured in DMEM supplemented with 10% fetal bovine serum (FBS) and 1% penicillin–streptomycin. MV4–11 cells were cultured in Roswell Park Memorial Institute-1640 (RPMI-1640) media (2 g/L glucose) containing 10% FBS and 1% penicillin-streptomycin.

Cell Viability Assay: Cell viability in MV4–11 was evaluated using the Cell Counting Kit-8 (CCK-8, GLPBIO Technology, Montclair, CA, USA). Cells were seeded at a density of 5×10^3 cells per well in 96-well plates and exposed to the test compounds at a concentration of 10 μM for 48 h. Following the incubation with compounds, 20 μL of the CCK-8 reagent was dispensed into each well at the appropriate time points. A 4 h incubation ensued, post which the OD was recorded using the same microplate reader (PE EnVision, Walpole, MA, USA) at an absorbance wavelength of 450 nm.

Western Blot Analysis: Western blot analysis was performed on MV4–11 cells. Briefly, cells were extracted with a lysate of RIPA and phenylmethylsulfonyl fluoride (PMSF; Beyotime, Shanghai, China) mixed at a ratio of 100:1. Protein concentration was determined using the BCA protein detection kit. Equal amounts of protein were then subjected to polyacrylamide gel electrophoresis (PAGE) and electrophoretic transfer to polyvinylidene difluoride membranes (activated with methanol for 5 min in advance). The membrane was then blocked with blocking buffer (Beyotime) for 0.5–1 h. Membranes were probed with the indicated primary antibody overnight at 4 °C and secondary antibody for 2 h at room temperature. After incubation with secondary antibody, blots were visualized using Super ECL Plus (Beyotime) and imaged by Chemiluminescence Apparatus (Bio-Rad, Berkeley, CA, USA), after which quantitative analysis was performed using ImageJ software (version: 1.8.0.112; National Institutes of Health, Bethesda, MD, USA). Primary antibodies: CDK6, Cyclin D1, Cyclin A, Bcl-2, p53, caspase-8, cleaved caspase-8, cleaved caspase-9 (all from Affinity, Liyang, China), tubulin (1:2000), and GAPDH (1:2000) (both from Proteintech, Shanghai, China). Secondary antibody: sheep anti-rabbit/mouse IgG H&L secondary antibody (horseradish peroxidase); goat anti-rabbit/mouse IgG H&L secondary antibody (horseradish peroxidase) (1:2000; ORIGENE, Beijing, China).

Detection of Apoptosis by Annexin V-FITC/PI Dual Staining Assay: MV4–11 cells were seeded in 6-well plates at a density of 4×10^5 cells/well and cultured for 24 h prior to drug treatment for 48 h. After incubation, the culture supernatant was collected, and adherent cells were detached using EDTA-free trypsin (to preserve calcium-dependent Annexin V binding activity). Cell pellets were obtained by centrifugation at 1500 rpm for 5 min, washed twice with PBS, and resuspended in 100 μL of 1 × Binding Buffer (containing

2.5 mM $CaCl_2$ as required for Annexin V-PS interaction). Subsequently, 5 µL of Annexin V-FITC and 5 µL propidium iodide (PI) were added (final ratio: Binding Buffer: Annexin V-FITC: PI = 100:5:10), followed by 15 min of incubation at room temperature in the dark (to prevent fluorochrome degradation). The reaction was terminated by adding 400 µL of 1 × Binding Buffer, and the stained cells were transferred to flow cytometry tubes for immediate analysis.

Cell Cycle Analysis by Propidium Iodide (PI) Staining: MV4−11 cells were seeded in 6-well plates at a density of 4×10^5 cells/well and cultured for 24 h prior to drug treatment for 24 h. Cells were harvested using EDTA-containing trypsin (to ensure complete detachment) and centrifuged at 1200 rpm for 5 min. The cell pellet was gently resuspended in 2 mL PBS and centrifuged again to remove supernatant. While continuously vortexing, ice-cold 80% ethanol (pre-chilled to −20 °C) was added dropwise for cell fixation, followed by overnight storage at 4 °C. The next day, fixed cells were centrifuged to remove ethanol, washed three times with PBS, and stained with 10 µL RNase A (to degrade RNA) and 500 µL PI staining solution (1:1000 dilution in PBS) for 30 min at room temperature in the dark (to prevent fluorochrome degradation). The cell suspension was then transferred to flow cytometry tubes for analysis.

Angiogenesis Assays: Prior to the experiment (24 h before), 24-well plates and pipette tips were pre-chilled at 4 °C, while Matrigel was thawed overnight at 4 °C. HUVECs were serum-starved for 24 h in serum-free medium before seeding. Each well was coated with 20 µL of pre-chilled Matrigel, which was evenly distributed and allowed to polymerize at 37 °C for 30 min. Subsequently, 1.5×10^5 cells were seeded per well. Tube formation was monitored and recorded at 3 h, 9 h, and 12 h post-seeding. Quantitative analysis of vascular network parameters, including formation area, branch points, and tube length, was performed using ImageJ software.

Subcutaneous Human Leukemia Xenograft Model in BALB/c Nude Mice: Following one-week acclimatization, female BALB/c nude mice received a 200 µL subcutaneous injection of human acute myeloid leukemia MV4-11 cells (washed in serum-free RPMI-1640, resuspended at 1×10^7 cells/mL) into the right axillary region. The cells were premixed 1:1 (v/v) with Matrigel® to establish xenografts. Palpable tumors developed within one week. Tumor volume ($V = L \times W^2/2$) was calculated from caliper measurements of longitudinal (L) and transverse (W) diameters. Upon volume stabilization, mice were randomized into four groups (n = 6): Vehicle Control (equivalent volume vehicle), Positive Control (Cyclophosphamide 40 mg/kg, p.o.), Low-Dose (test compound 20 mg/kg, p.o.), and High-Dose (test compound 40 mg/kg, p.o.). Treatments were administered daily for 14 days, with daily monitoring of health status (activity, alertness, weight, food/water intake). Post-treatment, mice were euthanized by cervical dislocation; tumors and major organs were aseptically excised for immediate wet weight determination.

Supplementary Materials: The following supporting information can be downloaded at: https://www.mdpi.com/article/10.3390/md24020063/s1. Figure S1: ^{1}H Spectrum of compound deschloro-phorbazole; Figure S2: ^{13}C Spectrum of compound deschloro-phorbazole; Figure S3: ^{1}H Spectrum of compound 3; Figure S4: ^{13}C Spectrum of compound 3; Figure S5: ^{1}H Spectrum of compound 4; Figure S6: ^{1}H Spectrum of compound 6; Figure S7: ^{1}H Spectrum of phorbazole C; Figure S8: ^{13}C Spectrum of phorbazole C; Figure S9: ^{1}H Spectrum of compound B1; Figure S10: ^{13}C Spectrum of compound B1;Table S1: Kinase selectivity profile of **B1**.

Author Contributions: Conceptualization, methodology, software, validation, formal analysis, investigation, data curation, visualization, X.C., L.Z., J.H., and X.J.; writing—original draft preparation, X.J.; writing—review and editing, M.S., Y.G., and X.J.; resources, supervision, project administration, funding acquisition, M.S., Y.G., and X.J. All authors have read and agreed to the published version of the manuscript.

https://doi.org/10.3390/md24020063

Funding: This research was funded by the National Natural Science Foundation of China (Grant no. 82304372), the Key R&D Program of Shandong Province (2025CXPT012, 2024CXPT029), and the Natural Science Foundation of Shandong Province (ZR2022QH139).

Institutional Review Board Statement: The animal study protocol was approved by the Ethics Committee of Yantai Institute of Materia Medica on 15 October 2024 (Approval Number: 20241015-01).

Data Availability Statement: The original contributions presented in this study are included in the article/Supplementary Material. Further inquiries can be directed to the corresponding authors.

Conflicts of Interest: The authors declare no conflicts of interest.

Abbreviations

The following abbreviations are used in this manuscript:

AML	Acute myeloid leukemia
HDAC	Histone deacetylase
MNK	MAP kinase-interacting kinases
eIF4E	Eukaryotic initiation factor 4E
NCS	N-chlorosuccinimide
HUEVC	Human umbilical vein endothelial cells
CTX	Cyclophosphamide
TGI	Tumor growth inhibition
LAH	Lithium aluminum hydride
PDGFRα	Platelet-derived growth factor receptor alpha

References

1. Hansen, K.O.; Andersen, J.H.; Bayer, A.; Pandey, S.K.; Lorentzen, M.; Joergensen, K.B.; Sydnes, M.O.; Guttormsen, Y.; Baumann, M.; Koch, U.; et al. Kinase Chemodiversity from the Arctic: The Breitfussins. *J. Med. Chem.* **2019**, *62*, 10167–10181. [CrossRef] [PubMed]
2. Chen, J.; Lv, S.; Liu, J.; Yu, Y.; Wang, H.; Zhang, H. An Overview of Bioactive 1,3-Oxazole-Containing Alkaloids from Marine Organisms. *Pharmaceuticals* **2021**, *14*, 1274. [CrossRef]
3. Rudi, A.; Stein, Z.; Green, S.; Goldberg, I.; Kashman, Y.; Benayahu, Y.; Schleyer, M. Phorbazoles A-D, novel chlorinated phenylpyrrolyloxazoles from the marine sponge Phorbas aff. clathrata. *Tetrahedron Lett.* **1994**, *35*, 2589–2592. [CrossRef]
4. Nuzzo, G.; Ciavatta, M.L.; Kiss, R.; Mathieu, V.; Leclercqz, H.; Manzo, E.; Villani, G.; Mollo, E.; Lefranc, F.; D'Souza, L.; et al. Chemistry of the nudibranch Aldisa andersoni: Structure and biological activity of phorbazole metabolites. *Mar. Drugs* **2012**, *10*, 1799–1811. [CrossRef] [PubMed]
5. Reierth, I.A.N.; Guttormsen, Y.; Andersen, J.H.; Hansen, E.H.; Abdelhady, A.M.; Langer, M.K.; Haug, B.E.; Bayer, A.; Petit, G.A. Investigation of the histone deacetylase inhibitor potential of phorbazole analogues. *Bioorg. Med. Chem.* **2026**, *133*, 118489–118501. [CrossRef] [PubMed]
6. Jin, X.; Li, M.; Qiu, T.; Yu, R.; Jiang, T. Design, Synthesis and Evaluation of Novel Phorbazole C Derivatives as MNK Inhibitors through Virtual High-Throughput Screening. *Mar. Drugs* **2022**, *20*, 429. [CrossRef]
7. Radspieler, A.; Liebscher, J. Total synthesis of phorbazole C. *Tetrahedron* **2001**, *57*, 4867–4871. [CrossRef]
8. Loughlin, W.A.; Muderawan, I.W.; McCleary, M.A.; Volter, K.E.; King, M.D. Studies towards the synthesis of phorbazoles A-D: Formation of the pyrrole oxazole skeleton. *Aust. J. Chem.* **1999**, *52*, 231–234. [CrossRef]
9. Guttormsen, Y.; Fairhurst, M.E.; Pandey, S.K.; Isaksson, J.; Haug, B.E.; Bayer, A. Total synthesis of phorbazole B. *Molecules* **2020**, *25*, 4848. [CrossRef]
10. Muderawan, I.W.; Louglin, W.A.; Young, D.J. Synthesis of a New Phorbazole and Its Derivatives. *Synthesis* **2022**, *54*, 1395–1403. [CrossRef]
11. Gao, W.-C.; Wang, R.-L.; Zhang, C. Practical oxazole synthesis mediated by iodine from α-bromoketones and benzylamine derivatives. *Org. Biomol. Chem.* **2013**, *11*, 7123–7128. [CrossRef]
12. Maddox, S.M.; Nalbandian, C.J.; Smith, D.E.; Gustafson, J.L. A Practical Lewis Base Catalyzed Electrophilic Chlorination of Arenes and Heterocycles. *Org. Lett.* **2015**, *17*, 1042–1045. [CrossRef]
13. Xu, B.; Maimaitijiang, A.; Nuerbiyamu, D.; Su, Z.; Li, W. The Multifaceted Role of p53 in Cancer Molecular Biology: Insights for Precision Diagnosis and Therapeutic Breakthroughs. *Biomolecules* **2025**, *15*, 1088. [CrossRef]

14. Graff, J.R.; Konicek, B.W.; Lynch, R.L.; Dumstorf, C.A.; Dowless, M.S.; McNulty, A.M.; Parsons, S.H.; Brail, L.H.; Colligan, B.M.; Koop, J.W.; et al. eIF4E activation is commonly elevated in advanced human prostate cancers and significantly related to reduced patient survival. *Cancer Res.* **2009**, *69*, 3866–3873. [CrossRef] [PubMed]
15. Culjkovic, B.; Topisirovic, I.; Skrabanek, L.; Ruiz-Gutierrez, M.; Borden, K.L. eIF4E promotes nuclear export of cyclin D1 mRNAs via an element in the 3'UTR. *J. Cell Biol.* **2005**, *169*, 245–256. [CrossRef]
16. Pandey, P.; Khan, F.; Upadhyay, T.K.; Seungjoon, M.; Park, M.N.; Kim, B. New insights about the PDGF/PDGFR signaling pathway as a promising target to develop cancer therapeutic strategies. *Biomed. Pharmacother.* **2023**, *161*, 114491–114504. [CrossRef]
17. Liu, Z.-L.; Chen, H.-H.; Zheng, L.-L.; Sun, L.-P.; Shi, L. Angiogenic signaling pathways and anti-angiogenic therapy for cancer. *Signal Transduct. Target. Ther.* **2023**, *8*, 198–236. [CrossRef] [PubMed]
18. Jin, X.; Yu, R.; Wang, X.; Proud, C.G.; Jiang, T. Progress in developing MNK inhibitors. *Eur. J. Med. Chem.* **2021**, *219*, 113420–113436. [CrossRef] [PubMed]
19. Patel, S.A.; Nilsson, M.B.; Le, X.; Cascone, T.; Jain, R.K.; Heymach, J.V. Molecular mechanisms and future implications of VEGF/VEGFR in cancer therapy. *Clin. Cancer Res.* **2023**, *29*, 30–39. [CrossRef]
20. Li, X.; Zhou, J.; Wang, X.; Li, C.; Ma, Z.; Wan, Q.; Peng, F. New advances in the research of clinical treatment and novel anticancer agents in tumor angiogenesis. *Biomed. Pharmacother.* **2023**, *163*, 114806–114821. [CrossRef]
21. Haouas, H. Angiogenesis and acute myeloid leukemia. *Hematology* **2014**, *19*, 311–323. [CrossRef] [PubMed]
22. Fiedler, W.; Staib, P.; Kuse, R.; Dührsen, U.; Flasshove, M.; Cavalli, F.; Hossfeld, D.K.; Berdel, W.E. Role of angiogenesis inhibitors in acute myeloid leukemia. *Cancer J.* **2001**, *7*, S129–S133. [PubMed]

Disclaimer/Publisher's Note: The statements, opinions and data contained in all publications are solely those of the individual author(s) and contributor(s) and not of MDPI and/or the editor(s). MDPI and/or the editor(s) disclaim responsibility for any injury to people or property resulting from any ideas, methods, instructions or products referred to in the content.